JOURNAL OF AIRCRAFT
Vol. 42, No. 5, September–October 2005

Biologically Inspired Fixed-Wing Configuration Studies

Barry S. Lazos*
NASA Langley Research Center, Hampton, Virginia 23681

Through the evolution of natural flight systems, it is expected that many have been optimized to provide enhanced efficiency. With this in mind the current study was conducted to determine whether flight configurations found in nature might be appropriately applied to fixed-wing mechanical flight systems to provide performance improvements through energy savings. Four different biologically inspired wings were designed and experimentally tested against a planar elliptic configuration used as a baseline. Two of the configurations show performance improvements over the baseline, using two different comparison techniques. Surface oil flow visualizations at the wingtips highlight differences that provide insight into the flow physics of the improvements.

Introduction

IT is widely believed that the evolutionary history of birds began with the specimen *Archaeopteryx* some 150 million years ago in the Late Jurassic.[1,2] Fishes, however, have a much longer history, with vertebrates first appearing in the fossil record during the late Cambrian Period with the specimen *Anatolepis*, some 500 million years ago.[3,4] Evolutionary theory presumes natural selection through survival of the fittest, where survivability depends on many factors such as food source, the ability to reproduce, and available habitat. With this in mind and given the length of time birds and fishes have existed, it is expected that avian and marine creatures have adapted their morphologies over time to survive within specific niches. Some of these adaptations are hypothesized to affect mobility efficiencies, reducing energy requirements and increasing maximum and sustainable speeds.

Human observations of the success of natural flyers apparently influenced the design of the first flying machines, because many incorporated avian morphological features.[5] Both fixed- and flapping-wing vehicles were designed and tested. Yet, for the most part, direct implementation of these "natural" features resulted in disaster. After the first successful flights, aircraft configuration began an evolution of its own with designers attempting to improve lift and drag performance as well as stability and control characteristics. One particularly noteworthy improvement is attributed to a theory developed by Munk[6] in 1923. It predicts that, for planar wing configurations, elliptic wing loading is the best at reducing induced drag. According to classical wing theory, the induced drag for an elliptically loaded wing is

$$C_{D,i} = C_L^2 \big/ \pi A \tag{1}$$

where C_L is the lift coefficient, $A = b^2/S$ is the aspect ratio, b is the wingspan, and S is the wing planform area. However, because all planar wing s do not perform to the highest standard of an elliptically loaded wing, an efficiency rating known as the span efficiency factor, e, is used to quantify a wing's induced drag performance. This efficiency factor is defined as $e = C_L^2/\pi A C_{D,i}$. According to Munk's theory, the efficiency, e, of an elliptically loaded planar wing is unity. However, because Munk's theory pertains only to planar wings, others have theorized that additional efficiency improvements can be made if nonplanar configurations are considered.

Likely some of the most radical nonplanar wing designs came from the work of Cone,[7] who developed quantitative theoretical procedures for the evaluation of induced drag benefits for arbitrary wing configurations. Some of the configurations he considered were similar to those found in nature and some provided efficiencies approaching 1.5. However, Cone's theoretical analysis was performed using potential theory, which means that viscous effects were not accounted for. Considering this and other parameters important in wing design, Cone commented that "the possibility of realizing net efficiency gains with nonplanar wings depends critically upon the ability to construct such forms with sufficiently low structural weights and physical surface areas, as compared with flat wings." These two points are important to keep in mind when considering advanced wing configurations for induced drag reduction. First of all, a theoretical configuration may show significant induced drag benefits but result in intolerable wing root bending moments. Second, a balancing act must be played in order to produce a wing configuration that has a net drag improvement. While there are likely many nonplanar wing configurations that will provide reductions in induced drag, the increase in surface area at constant aspect ratio and planform area will certainly produce more skin friction drag. Clearly, designing a new wing with an overall drag benefit that is feasible for use on an actual aircraft is not an easy task.

The induced drag of a configuration, as discussed above, is a component of drag entirely independent of viscous effects. With viscous effects included, another term, also proportional to C_L^2, results due to parasite drag.[8] The combination of this term and the induced drag term results in what is called lift-dependent drag. The list of passive and active techniques for lift-dependent drag reduction is quite large and Henderson and Holmes[9] and Rokhsaz[10] have performed reviews of much of the work. Two techniques should be mentioned here, however, because of their biological inspiration. The first is a planar configuration with an elliptic chord distribution and a planform crescent shape (wing 3 in Fig. 1). A similar version of this configuration is often observed in the wings of many fast-flying birds and in the caudal fins of many fast-swimming fish. An efficiency study of this wing configuration was first performed by van Dam[11] using a panel method that allowed for wake relaxation and vortex rollup. The results indicated that although the lift-curve slope was slightly reduced, there was a significant reduction in induced drag, resulting in an efficiency improvement of as much as 8.8% over a classical elliptic planform with an unswept quarter chord (wing 1 in Fig. 1). In a later report, however, van Dam et al.[12] performed a wind tunnel investigation and found that the lift-to-drag (L/D), improvement of the crescent configuration over the classical unswept elliptic planform was only 1 to 2%.

The second biologically inspired wing modification designed for lift-dependent drag reduction is the wingtip sail. This tip modification was inspired by the wingtips of soaring landbirds, which are discussed subsequently. (A planform view of the splayed tip feathers on a condor is shown in Fig. 2.) Normally three or four sails are positioned on the wingtip at different chordwise locations and

Received 30 April 2004; revision received 8 October 2004; accepted for publication 6 November 2004.

*Research Scientist, Flow Physics and Control Branch, 1 E. Reid Street. Member AIAA.

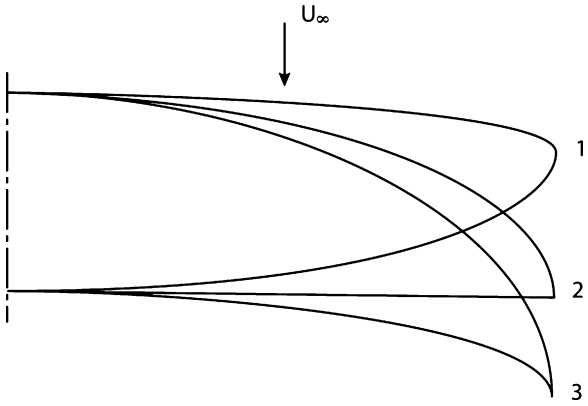

Fig. 1 Wing configurations studied by van Dam (Fig. 3 from Ref. 11).

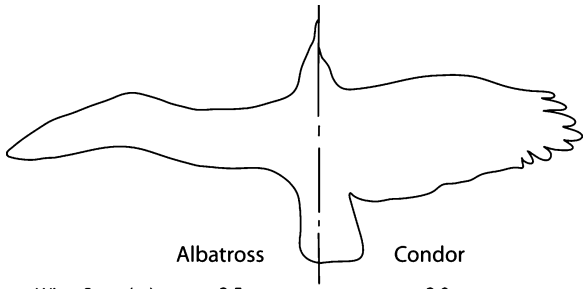

Fig. 2 Planform configuration comparison between soaring seabirds on the left and soaring landbirds on the right (taken from Fig. 3 of Ref. 16).

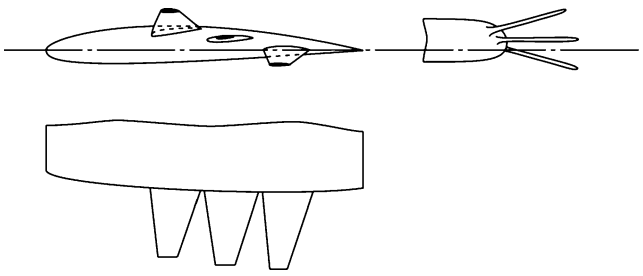

Fig. 3 Wingtip sails (Fig. 9 from Ref. 13).

each is rotated about the tip at an increasing angle as chordwise position is increased (Fig. 3). Wingtip sails are designed to take advantage of the upflow at the wingtip with each sail positioned to provide a thrust component that is predicted to more than offset the lift-dependent drag of the wing. A comprehensive review of much of the work performed on wingtip sails is presented by Spillman.[13] In this report the author states that flight tests using wingtip sails provided an improvement in lift-dependent drag by as much as 28%. The benefits, however, are stated to be angle of attack– and velocity-dependent. As angle of attack is increased beyond a certain point, separation effects on the sails dramatically reduce their effectiveness. As airspeed is increased (lift coefficient is reduced), Spillman notes that the skin friction drag penalty begins to exceed the benefit in lift-dependent drag provided by the sails. This latter effect of overwhelming skin friction due to increased surface area is precisely what Cone[7] warned against.

Although it is often considered that the predominant source of propulsion for birds is wing flapping, soaring techniques are also used and are especially energy-efficient because little effort is required for maintaining a constant wing configuration during flight. (Refer to Ref. 14 for a thorough description of the different soaring techniques used by birds.) Two significantly different planform configurations are observed in birds noted for their soaring ability, as pointed out by Raspet.[15] These differences are clearly demonstrated in Fig. 2, taken from Ref. 16. On the left is the planform of a wandering albatross (*Diomedae exulans*), which is typical of soaring seabirds. On the right is the planform of a California condor (*Gymnogyps californius*), which is typical of soaring landbirds. The distinct differences are those of wing loading, aspect ratio, and tip configuration. Soaring seabirds have a sharp swept tip and higher aspect ratio, whereas soaring landbirds have splayed feathers at the tip and a lower aspect ratio.

In the current study, the wing morphology of soaring seabirds is chosen as the avian configuration of primary interest. The marine morphology chosen is that of the fins of fast-swimming fish. Wind tunnel tests were performed on four new wing configurations intended to reduce lift-dependent drag with respect to that of a baseline configuration. Each model was sting mounted and forces and moments were acquired through an angle of attack range. Oil-flow visualization studies were conducted to help determine some of the flow physics, especially at the wingtips. All models tested had the same aspect ratio and planform area; therefore any improvement in drag is expected to result from a lift-dependent drag improvement.

Facility, Models, and Data Acquisition

Experiments were conducted in the Basic Aerodynamics Research Tunnel at the NASA Langley Research Center. This facility is an open-circuit wind tunnel with a test section area of 28×40 in. and a length of 120 in. The facility was operated at a constant speed for all tests to yield a Reynolds number per foot of 10^6. Reference 17 provides detailed information on tunnel flow quality and indicates that turbulence levels are below 0.1% at near maximum freestream velocity.

Five different models were tested. All models were attached to the same centerbody and all had a wing planform area of 112 in.^{2} and a wingspan of 28 in. This resulted in an aspect ratio of 7 for each configuration. Here the wing reference area used to calculate the aspect ratio is the planform area of the wings alone (112 in.^{2}), excluding any area projected into the centerbody. This definition of aspect ratio was chosen because it was expected to better represent the geometry differences between the wings. The airfoil section used was the SD7032, a low-Reynolds-number airfoil designed to mitigate separation problems through the use of a bubble ramp. The maximum wind tunnel blockage for all models was approximately 2.7%.

The baseline configuration was a wing with an elliptic leading edge and a straight trailing edge (wing 2 in Fig. 1) . This configuration was chosen for the baseline because Smith[18] demonstrated, through detailed computational studies, that this planform provided an induced-drag efficiency factor closer to unity than any other planform tested with an elliptic chord distribution. The design of the other four wings tested relied on biological inspiration. The first was a nonplanar wing configured after the wing of a seagull in soaring flight and is designated the gull wing. An exact likeness was not achieved, however, because seagulls have a characteristically larger aspect ratio than that preferred in the present study. Modifications were made to produce the desired wing parameters. The second model was a planar wing configuration designed to represent a combination of the pectoral, dorsal, and caudal fins of a great white shark and is designated the shark wing. The great white shark was chosen to model because its associated Reynolds numbers are relatively high and information about this species was readily available through contacts with the Virginia Institute of Marine Sciences. The third model was configured like the baseline wing except that sine wave curvature was added to the leading edge. It was designated the wavy-leading-edge, or WLE, wing. The period and amplitude of the imposed sine wave were 2.0 and 0.2, respectively. This model was intended to represent morphologies such as the pectoral fin of a humpback whale, which has bumps along its leading edge, and the wavy leading edge on the head of the scalloped-head hammerhead shark. Watts and Fish[19] conducted a numerical study using a similar configuration and reported that the primary benefit of leading-edge bumps is most likely enhanced maneuverability through delayed stall. This characteristic was not investigated in the current study.

The final model was configured after a seagull in high-speed gliding flight and took into account the work of Cone.[7] This configuration is also nonplanar, with the curvature in the upstream view defined by a hyperelliptic equation, that is, an elliptic equation with an exponent greater than 2. The exact equation is given as

$$\left(\frac{z+4.727}{4.727}\right)^{2.5}+\left(\frac{y}{13}\right)^{2.5}=1 \tag{2}$$

where z (in.) is in the upward normal direction and y (in.) extends from root to tip. With the wing unfurled the leading-edge and trailing-edge curvatures in the planview are defined, respectively, by the following hyperelliptic equations:

$$\left(\frac{9.522-x}{9.522}\right)^{2.5}+\left(\frac{y}{15.121}\right)^{2.5}=1 \tag{3}$$

$$\left(\frac{4.727-x}{4.727}\right)^{2.5}+\left(\frac{y}{15.121}\right)^{2.5}=1 \tag{4}$$

where x (in.) is in the streamwise direction. This particular configuration was designated the HECS wing because of its characteristic hyperelliptic cambered span.

Model wings were constructed in a three-step process to produce a durable configuration. First, each was formed in SL 5180 resin using stereolithography. The resin wings were then sanded and molded in a pliable polyurethane. The final wing configurations were then cast in a stiff polyurethane that has a flexural modulus of 432 ksi and is more resistant to the adverse effects of humidity and ultraviolet light than SL 5180 resin. Models were constructed by attaching the left and right wings to a centerbody cap. This allowed screw attachment of each model to the same aluminum centerbody, which was a generic cylindrical shape 2 in. in diameter with an elliptic nose cone. Figure 4 shows a perspective view of four of the models sting-mounted in the tunnel test section. Figure 5 is a perspective view of the WLE wing outside the tunnel but attached to the centerbody.

Force and moment data were acquired using a six-component strain gauge balance. Before each run, wind-off tares were acquired by running the model through an angle-of-attack range. This provided an in situ measure of the balance electrical zeros, model static weight, and center-of-gravity location. Balance data were acquired through an angle of attack range of −5 deg to the maximum for each model in increments of 1 deg. The maximum angle of attack varied between 8 and 12 deg for each model due to balance or flutter constraints. For each reading of the balance, data were acquired at a rate of 300 samples per second, with 28 sets of 1000 samples acquired to provide a good mean measurement. Temperature and pressure data were acquired simultaneously with the balance data at the same sample rate to accurately calculate dynamic pressure at each angle of attack.

Oil-flow visualizations were conducted with each model at an angle of attack of 8 deg. This angle of attack was chosen rather arbitrarily as a midpoint in the full angle of attack range where sufficient lift was produced to show distinguishing surface-flow characteristics. The technique involved mixing kerosene and titanium dioxide powder together in a ratio that produced a suspension thick enough to effectively visualize the surface-flow line characteristics but thin

Fig. 5 Perspective view of wavy leading edge (WLE) wing.

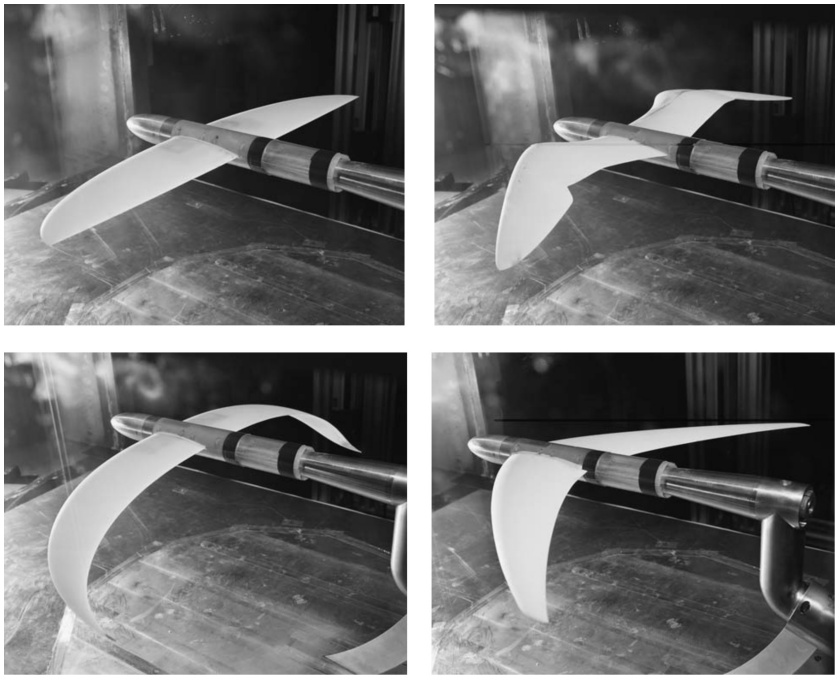

Fig. 4 Model configurations from upper left clockwise: baseline wing, gull wing, shark wing, HECS wing.

enough to flow adequately at all locations on the wing, considering that the shear stress varied across the wing surface. The suspension was painted on the upper and lower surfaces of each wing with a brush. The tunnel was then quickly brought up to operating speed and allowed to run until the kerosene had completely dried and the flow lines were readily apparent. Digital video was used to record the dynamic features of the oil flow during test runs. Cameras were positioned both above the test section, to image the suction side of the models, and alongside the test section, to obtain closeups of the suspension flow dynamics at the wingtips. After each run the models were removed from the test section and the resulting surface-flow line features were recorded using high-resolution digital photography.

Experimental Accuracy and Error Estimation

An accurate measure of the angle between the model and the horizontal can be difficult unless an accelerometer is located within the model. For the present study the accelerometer was attached to the sting support. To account for deflections in the balance due to aerodynamic loads, deflection coefficients obtained from the balance calibration were used. Both normal-force and pitching-moment coefficients were used in the correction and were given in units of degrees per pound and degrees per inch-pound, respectively.

Even with an accurate measure of the angle that the model makes with the horizontal, an accurate measure of the angle of attack is not guaranteed because the flow in the test section is likely to be at some angle to the horizontal. In order to account for this accuracy error

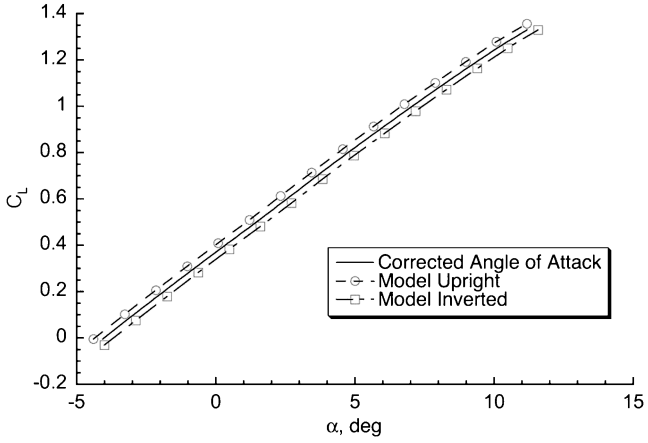

a) Baseline wing

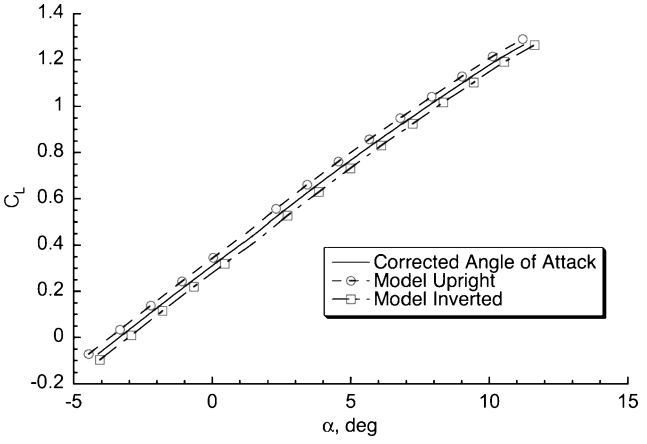

c) HECS wing

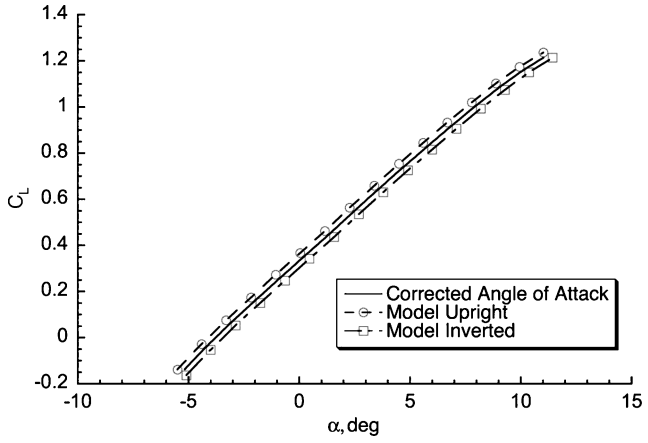

b) Gull wing

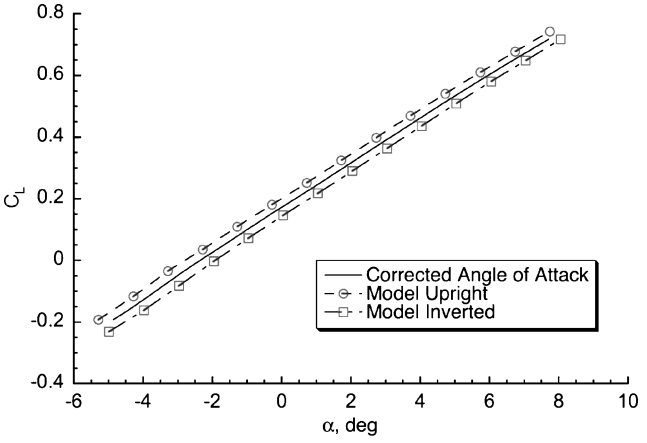

d) Shark wing

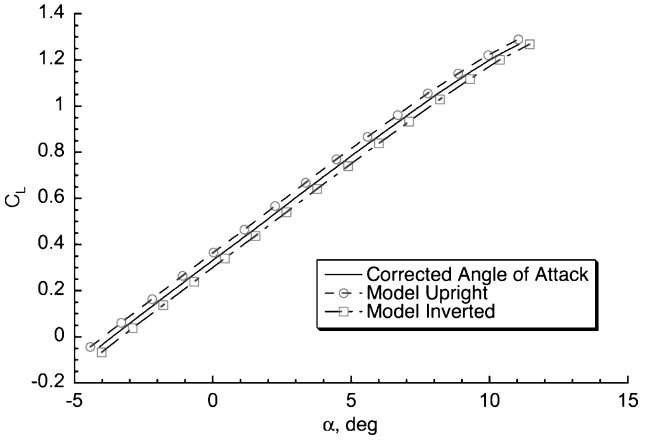

e) WLE wing

Fig. 6 Method of Barlow (Ref. 20) used to correct for tunnel upflow angle effects on angle of attack.

in the current study, the method of Barlow et al.[20] was used. Each model was run several times through the angle of attack range in both an upright and an inverted position. The mean lift coefficient was then plotted against the measured mean angle of attack for both the upright and inverted cases. The actual angle of attack was then determined at constant lift coefficient values by locating the mean between the upright and inverted cases. Figures 6a–6e show how this technique was used for each model and demonstrate the goodness of fit of the curve approximations to the experimental data. Drag coefficient values were corrected in a similar fashion by plotting lift coefficient versus mean drag coefficient for both the upright and inverted cases. A fourth-order polynomial was then fitted to the data, which provided a minor amount of smoothing. The actual drag coefficient was then determined as the mean between the polynomial curves running through the upright and inverted data. For the baseline, HECS, and WLE wings, the data points at an angle of attack of −5 deg were not considered in the calculation of the polynomial fit because they appeared to be outliers, as shown for the baseline case in Fig. 7a. Figures 7b–7e show similar plots for the other wing configurations and demonstrate the goodness of fit of the polynomial approximations to the experimental data.

Because plots are presented using mean values of the angle of attack and lift and drag coefficients, the scatter about the mean will be used to determine the precision error associated with the measure of each. Rather than considering measured values for each model separately, the 13 runs for the upright baseline model will be used. These data are expected to yield the best precision error characteristics because the runs were made at intervals throughout the tunnel

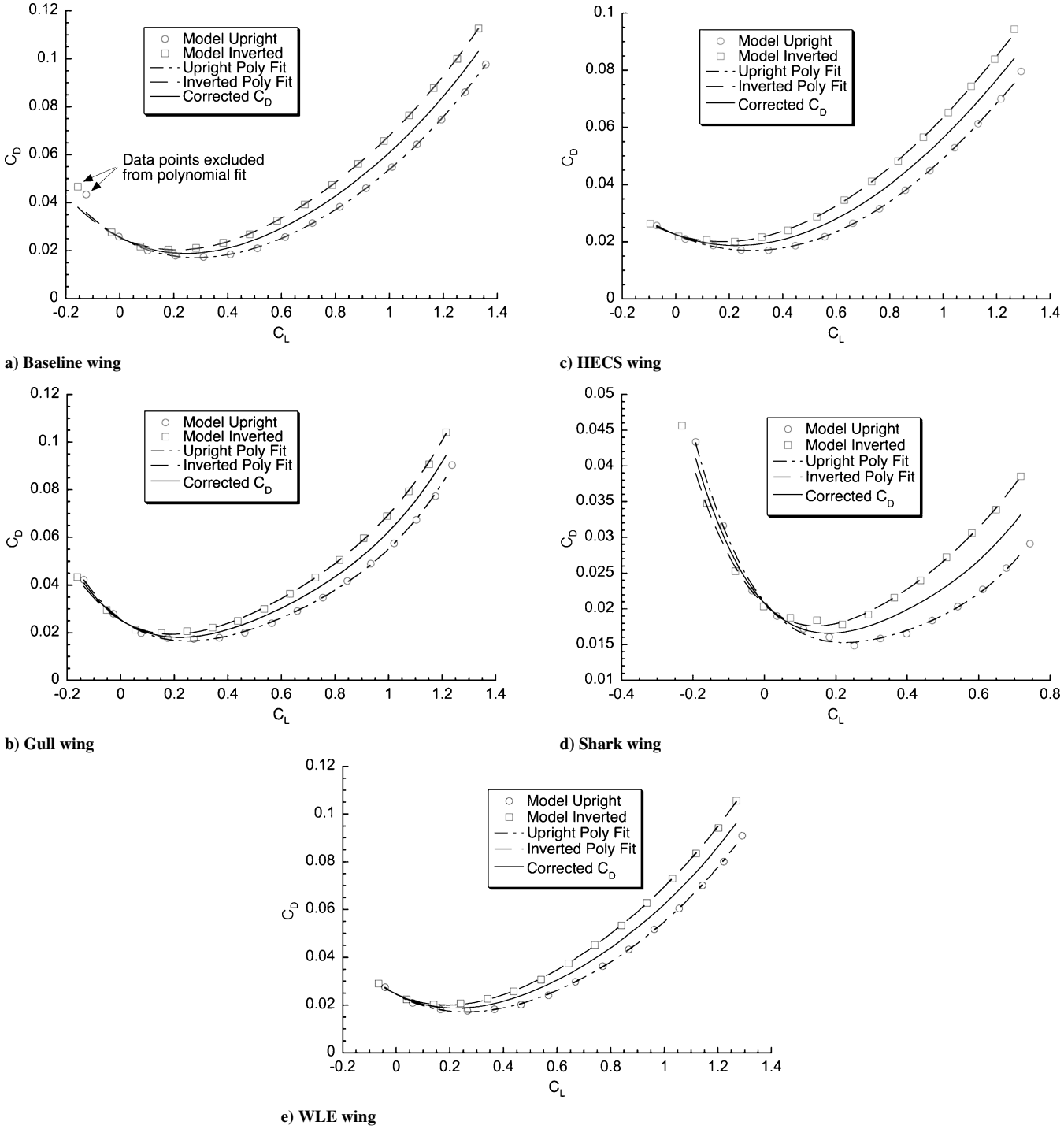

a) Baseline wing

c) HECS wing

b) Gull wing

d) Shark wing

e) WLE wing

Fig. 7 Method of Barlow (Ref. 20) used to correct for tunnel upflow angle effects on drag coefficient values.

entry to ensure measurement repeatability. In order to construct this analysis it is assumed that the possible precision error range is consistent at each measurement location. This provides a sample size of 208 points because for each of the 13 runs, data were acquired at 16 different model angles. Differences from the mean values of angle of attack, lift coefficient, and drag coefficient are plotted in histogram fashion in Figs. 8–10, respectively. It is readily apparent that the measurement distribution is nearly Gaussian in all three cases, as might be expected. A statistical analysis shows standard deviations in angle of attack, lift coefficient, and drag coefficient of 1.29×10^{-2} deg, 4.39×10^{-3}, and 6.15×10^{-4}, respectively.

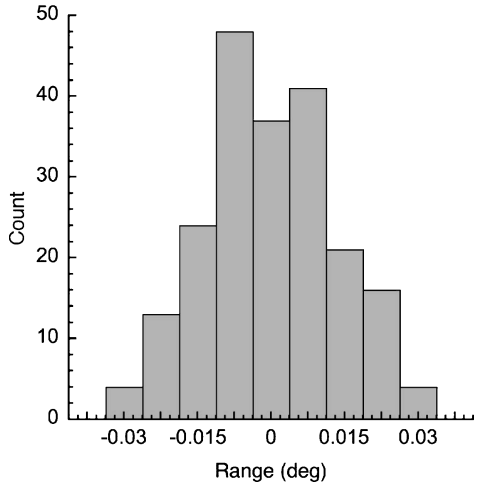

Fig. 8 Histogram of scatter about mean angle of attack.

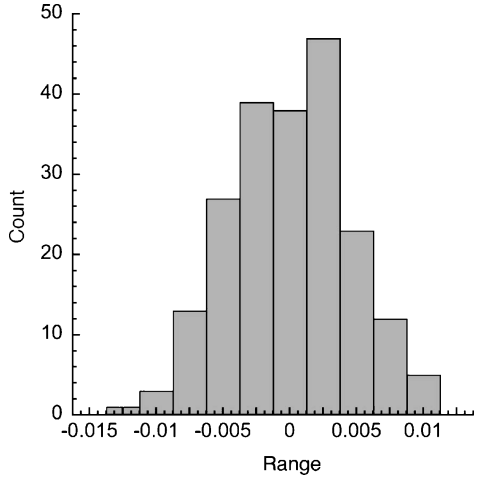

Fig. 9 Histogram of scatter about mean lift coefficient.

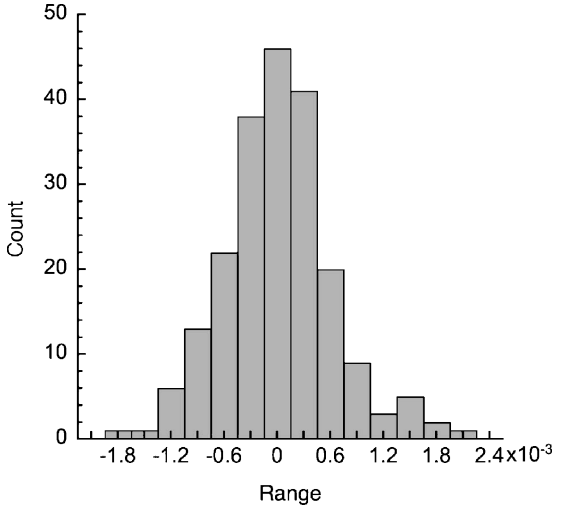

Fig. 10 Histogram of scatter about mean drag coefficient.

Results and Discussion

In the following plots, angle of attack and drag coefficient have been corrected to account for tunnel upflow angle according to the previously mentioned method of Barlow et al.[20] Therefore, only the polynomial representation of the corrected data is shown and the experimental data points representing the upright and inverted model conditions are omitted. Figure 11 shows a plot of angle of attack versus lift coefficient. The data show that the baseline (elliptic) wing provides more lift at all angles of attack than any other wing configuration. The HECS, WLE, and gull wings are comparatively close to the baseline wing in lift performance, whereas the shark wing far underperforms any of the wing models at all angles of attack. An explanation for this is provided by Lowry and Polhamus,[21] where potential theory is used to show that, with constant aspect ratio and Mach number, the lift curve slope decreases as the sweep angle increases. Table 1 lists the mean sweep angle of each wing configuration using

$$\Lambda_{\mathrm{TE}} = \tan^{-1}\left(\frac{x_{\mathrm{tip}} - x_{\mathrm{root}}}{b/2}\right) \tag{5}$$

where b was defined previously as the wingspan. Because, for the present experiment, aspect ratio and wing planform area are calculated without extending the wing into the fuselage, the same practice is used for the sweep angle calculations.

In considering the results in Table 1, it must be remembered that the three wings with mean sweep are swept very unconventionally, as demonstrated in Fig. 4. It must also be noted that rather than rotating the wings about the root, as is normally done, "wing sweep" is produced by translating the airfoil cross sections of the wings in the downstream direction from root to tip. In other words, the cross-sectional airfoil shape of the wings remains in the streamwise direction.

The drag curves shown in Fig. 12 indicate that the baseline wing has consistently higher drag values than any other configuration for all angles of attack greater than zero. By far the most significant improvement in drag is seen with the shark wing, where the drag

Table 1 Model mean sweep angle

Wing model	Mean sweep angle, Λ_{TE}, deg
Baseline	0.00
Gull	2.53
HECS	19.98
Shark	30.89
WLE	0.00

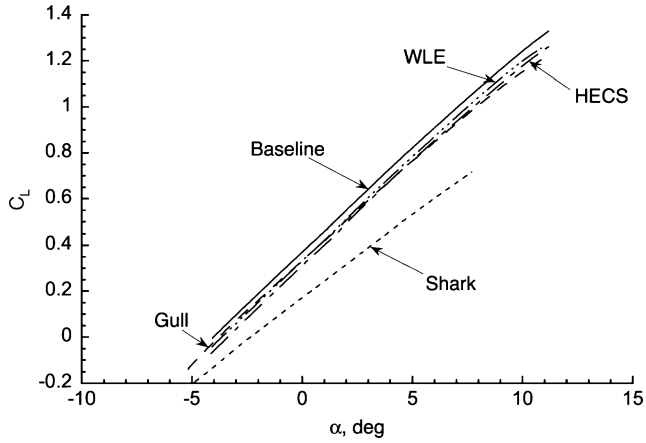

Fig. 11 Lift curves for each model configuration (data corrected for tunnel upflow angle).

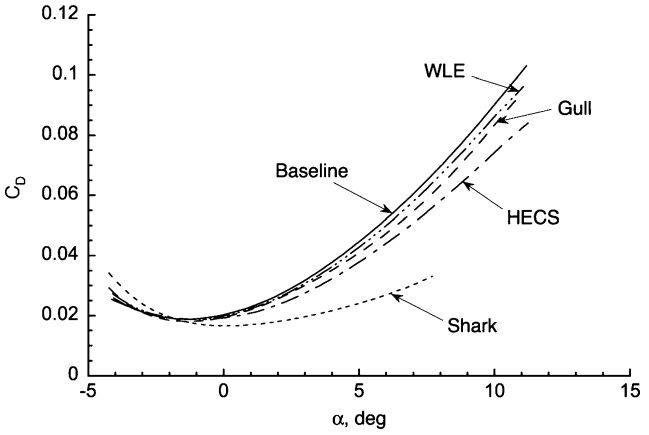

Fig. 12 Drag curves for each model configuration (data corrected for tunnel upflow angle).

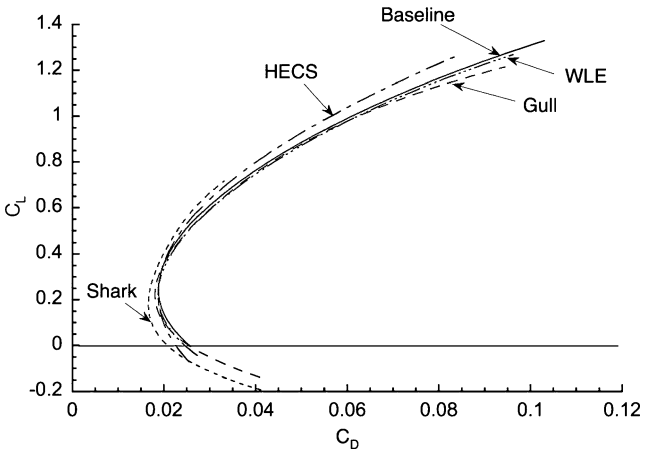

Fig. 13 Drag polar for configurations tested (data corrected for tunnel upflow angle).

value at an angle of attack of 5 deg, for example, is 45% lower than the baseline value at the same angle of attack. The HECS wing is seen to be the second best contender, with a drag value 14% lower than the baseline at an angle of attack of 5 deg.

A good indicator of wing performance is the span efficiency factor, e, defined previously in the Introduction. This value is best determined with inviscid calculations for a symmetric wing configuration that does not include a centerbody. In the current experiment each configuration includes a centerbody and, of course, viscous effects cannot be neglected. Because the airfoil section used for the models is cambered, the appropriate relationship between the lift and drag coefficients can be expressed as

$$C_D = C_{D(\min)} + K\left(C_L - C_{L(\min\text{ drag})}\right)^2 \tag{6}$$

Here, the first term on the right-hand side of Eq. (6), $C_{D(\min)}$, represents the minimum parasite drag coefficient and can be determined from the drag polar (Fig. 13) by locating the point on each curve where the slope, $\mathrm{d}C_D/\mathrm{d}C_L$, is zero. This is the location where C_L equals $C_{L(\min\text{ drag})}$, making the second term in Eq. (6) vanish. Because wetted area affects the level of skin friction drag, and parasite drag includes skin friction drag, one may expect the smallest parasite drag coefficient for the wing of least surface area. The surface area of each wing was calculated using a surface area function in the CAD routine used to build the wings. Both $C_{D(\min)}$ and surface area values for each wing are shown in Table 2 along with percentage differences compared to the baseline wing. All surface area values are in inches squared and represent the surface area of one wing only.

The results in Table 2 show that the baseline wing and the WLE wing have nearly equal minimum drag coefficients, as may be expected, since they are very similar in design. What is rather unexpected, however, is that the HECS wing also has a $C_{D(\min)}$ value

Table 2 Minimum parasite drag coefficient from polar (Fig. 13)

Wing model	$C_{D(\min)}$	Percent difference ($C_{D(\min)}$)	Wing surface area, in^2	Percent difference (surface area)
Baseline	0.0188	0.0	114.206	0.0
Gull	0.0180	−4.3	117.911	3.2
HECS	0.0188	0.0	126.246	10.5
Shark	0.0166	−11.7	115.373	1.0
WLE	0.0186	−1.1	114.095	−0.1

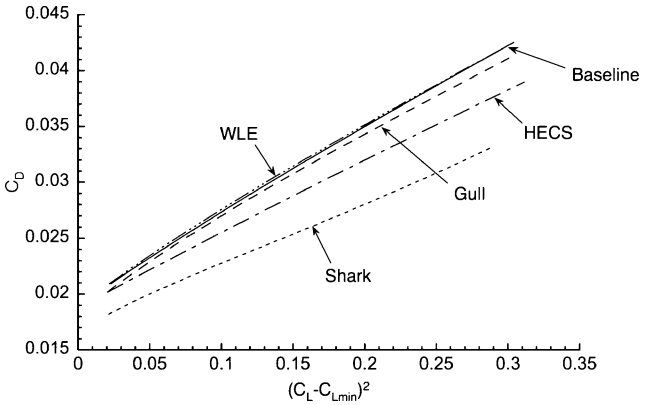

Fig. 14 Plots used to determine the drag due to lift coefficient, K, for each model configuration (data corrected for tunnel upflow angle). Data plotted for $0.4 \le C_L \le 0.7$.

equal to the baseline, whereas the value for the gull wing is lower. Also striking is the fact that $C_{D(\min)}$ for the shark wing is the lowest of all wing configurations. When the wetted surface area of each wing is considered, there appears to be no direct correlation between it and the value of $C_{D(\min)}$. This may not be the contradiction it seems, however, because parasite drag consists of both skin friction drag and pressure drag due to flow separation. From the results, one might expect that flow separation would play an important role in the values of $C_{D(\min)}$ for the current wing configurations.

Returning to Eq. (6), we can determine the inviscid span efficiency rating of each model by separating the constant K into its viscous and inviscid components of drag due to lift,

$$K = K_p + K_i/\pi A \tag{7}$$

Here K_i is the inviscid component constant whose inverse is the span efficiency rating, e. Taking the derivative of Eq. (6) with respect to $(C_L - C_{L(\min\text{ drag})})^2$ and plotting $(C_L - C_{L(\min\text{ drag})})^2$ versus C_D, values of K are determined from the slope of each curve as plotted in Fig. 14. With K known for each model, a value of K_p can be determined for the set of models by first substituting the right-hand side of Eq. (7) into Eq. (6) and differentiating with respect to $(C_L - C_{L(\min\text{ drag})})^2$:

$$\frac{\mathrm{d}C_D}{\mathrm{d}(C_L - C_{L(\min\text{ drag})})^2} = K_p + \frac{K_i}{\pi A} \tag{8}$$

If we consider airfoil data for the SD7032,[22] there is no induced drag associated with it because the aspect ratio goes to infinity. Therefore, the second term on the right-hand side of Eq. (8) vanishes. When $(C_L - C_{L(\min\text{ drag})})^2$ is plotted versus C_D using the airfoil data with $0.167 \le C_L \le 1.0$, the slope provides an approximate value for K_p of 0.0154. Admittedly, it is a stretch to expect that a single value of K_p determined using two-dimensional airfoil data can be applied to the set of three-dimensional models, but here we are interested in determining comparative values of K_i. Table 3 shows the values of K, K_i, and the efficiency rating, e, for each model configuration.

The efficiency ratings indicate that all wings performed better than the baseline wing. For the new wing configurations, the WLE wing was the worst performer, with the next best being the gull wing. The shark wing was the best performer, with a 65.4% efficiency improvement over the baseline wing. The HECS wing was the next best performer with a 30.4% improvement.

Table 3 Configuration efficiency ratings from experimental data

Wing model	K	K_i	Efficiency rating, e	Percent difference
Baseline	0.0768	1.3503	0.7058	0.0
Gull	0.0744	1.2975	0.7707	9.2
HECS	0.0648	1.0864	0.9205	30.4
Shark	0.0544	0.8576	1.1677	65.4
WLE	0.0767	1.3481	0.7418	5.1

Table 4 Maximum lift-to-drag values and percentage difference from baseline value

Wing model	$(L/D)_{max}$	Percent difference
Baseline	20.54	0.0
Gull	19.88	−3.2
HECS	21.36	4.0
Shark	22.43	9.2
WLE	19.80	−3.6

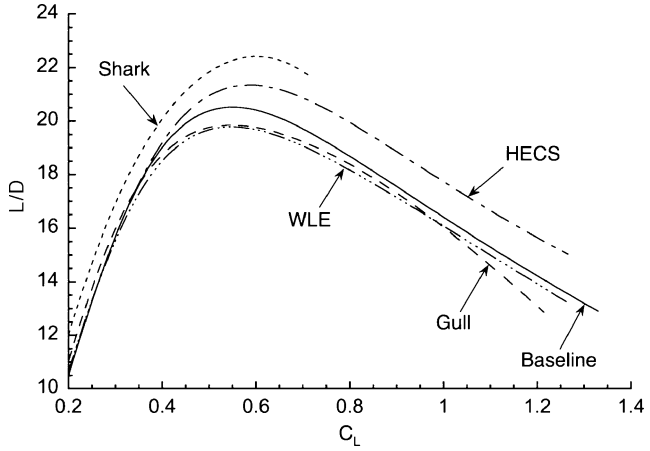

Fig. 15 Lift-to-drag comparison for configurations tested (data corrected for tunnel upflow angle).

Probably one of the best methods to compare wing performance using experimental data is to consider maximum lift-to-drag ratio. Figure 15 shows lift-to-drag for each wing configuration plotted against lift coefficient. This figure represents a range or endurance comparison depending on whether the aircraft is propeller or turbojet driven. From the figure, the shark wing is the best performer, followed by the HECS wing. The figure also shows that the HECS wing provides a much higher lift-to-drag ratio over a wider range of lift coefficient. This would equate to an improved operating range for an aircraft during cruise where the lift coefficient changes due to altitude changes and/or fuel use. Table 4 shows the maximum lift-to-drag values for each wing as well as the percentage difference relative to the baseline wing.

This method of wing comparison provides somewhat different results than the data in Table 3. Here, the gull wing and the WLE wing perform about 3% worse than the baseline wing. However, the shark wing is still identified as the best performer, with the HECS wing showing the second best performance.

The two comparisons above clearly indicate the performance benefits of the shark and HECS wings. It should be noted, however, that during testing, the wingtips of each model were seen to deflect increasingly as angle of attack was increased. Unfortunately the amount of deflection was not recorded. Only speculation can be made about the effect of wingtip deflection on the performance of each model. In general, there are two ways wingtip deflection can alter wing performance: through changes in aspect ratio or geometric twist. Aspect ratio might increase during loading in either the HECS wing or the gull wing due to their natural anhedral state, as shown in Fig. 16. This is opposed to the other wing configurations, which are planar. These configurations would experience a decrease in aspect

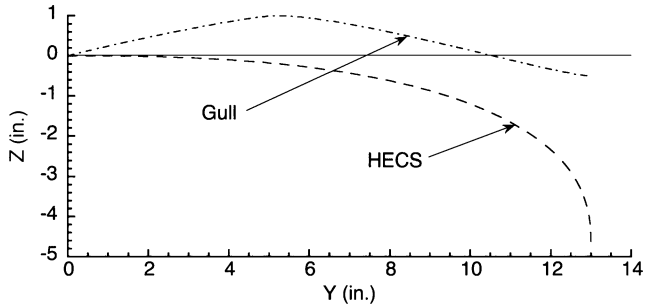

Fig. 16 Curvature of HECS and gull wings (streamwise view).

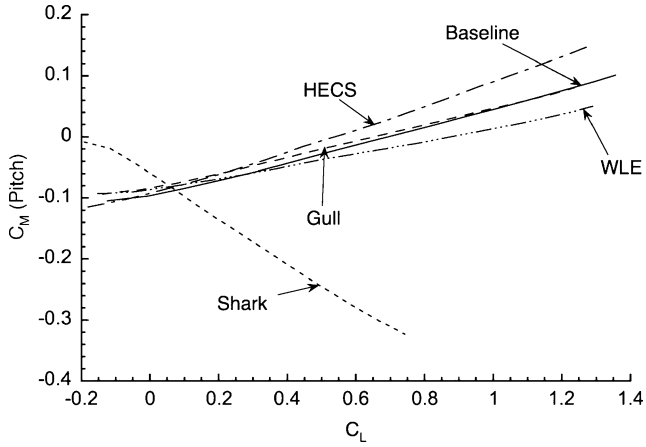

Fig. 17 Pitching-moment coefficient for each configuration tested (displayed curves are for the model upright case only). Moment taken about model center of gravity.

ratio as aerodynamic loading increased. If aspect ratio changes had a significant effect on wing performance in the current study, it is expected that Fig. 15 would show signs of it. For example, consider the performance of the HECS wing and baseline wing at the higher lift coefficients, as shown in the figure. If aspect ratio changes played a significant role in the enhanced performance of the HECS wing, one would not expect the constant, nearly equal slopes of the curves shown for each wing. Unfortunately, the effects of geometric twist on wing performance are harder to access with the current data. In the design of a wing, twist is often included to improve its lift distribution and bring its efficiency rating closer to unity. To the author's knowledge, however, twist has never been used in an attempt to improve a wing's efficiency rating beyond unity, nor is it speculated that it can be. As mentioned previously, the baseline wing in the current study was chosen as a result of computational studies[18] that show it has an inviscid efficiency value very close to unity. Since both the shark wing and the HECS wing demonstrate a lift-to-drag improvement over the baseline wing, it is expected that their inviscid efficiency values are greater than unity. Clearly it is difficult to access how tip deflection affected the performance characteristics of the current wing configurations; therefore, this issue should be addressed in further studies at a future date.

The pitch characteristics of a wing are important to consider in evaluating efficiency, because it is usually desirable to fly a configuration at a lift coefficient that provides either maximum range or maximum endurance. If the pitching moment at this lift coefficient is large, the trim settings may result in significant reduction or elimination of any performance improvements observed in the experimental evaluation of the wing. Figure 17 shows a plot of the lift coefficient versus the pitching-moment coefficient for each configuration tested. Here, the pitching moment is taken about the model center of gravity. Because the current test configurations have no empennage, limited information can be gathered from the plot. However, when the magnitude and sign of each pitch curve slope, are considered, it is apparent that all the current configurations are slightly unstable in pitch except for the shark wing model, which

has a rather severe pitch recovery characteristic. At a lift coefficient of about 0.575, a value corresponding to an average maximum lift-to-drag value for all wings, Fig. 17 shows that all wings have a nearly zero pitching moment except for the shark wing, which has a pitching-moment coefficient of nearly −0.28. Such strong pitch recovery for the shark wing may drastically reduce or eliminate observed performance improvements.

Oil-flow visualization studies were conducted in order to gain some insight into the flow physics associated with the observed performance improvements in the wing configurations. Figures 18a–18c show the oil-flow features on the suction side at the tips of the baseline, HECS, and shark wings, respectively, at an angle of attack of 8 deg. Other wing configurations will not be discussed because they show no performance improvement. Each of the figures shows the existence of a laminar separation bubble, indicated by the line of separation just downstream of the leading edge, and the following reattachment line. Flow lines on the baseline wing in Fig. 18a indicate a conventional tip vortex structure identified by the separation line at the tip edge and the inboard reattachment line. Vortex rotation indicated by these markings would produce the expected downwash behind the wing. Figures 18b and 18c show that the HECS wing and shark wing have a much more complicated surface flow line structure at the wingtip. Both wings have a very distinct line of separation just ahead of the trailing edge. Along these lines, oil suspension is observed to travel toward the wingtips. Both wings also have a region of flow recirculation at the tips. On the HECS wing, clockwise flow can be observed within this region and suspension is observed to become entrained along a line of separation, as indicated in Fig. 18b. On the shark wing, no internal flow could be discerned in the recirculation region. Just downstream of the recirculation region on the HECS and shark wings, careful analysis of video data indicated a line of attachment. It is hypothesized that this attachment line, along with the separation line just inboard of it, identifies a counterclockwise vortex structure when viewed from behind the wing in the upstream direction. A line of separation outboard of the line of attachment at the leading edge of each wing (not seen in the figures) suggests that this counterclockwise vortex persists alongside one of opposite sign to form a counter-rotating vortex pair at the tip of each wing.

To simulate higher-Reynolds-number conditions, a line of #46 grit, $\frac{1}{8}$ in. wide, was added to the baseline, HECS, and shark wings. The grit line was positioned so that it was just upstream of the line of separation marking the beginning of the separation bubble observed along the leading edges of the smooth wings. To attach the grit, a light coat of spray adhesive was applied to the wing surface and grit was sprinkled onto the adhesive line. Oil-flow visualization was performed downstream of the grit at angles of attack of 0 and 8 deg to ensure that the separation bubble no longer persisted on the suction surface of the wings. The lift-to-drag results of the baseline, HECS, and shark wings with trip grit applied are shown in Fig. 19 with the same ordinate scale as used in Fig. 15. Figure 19 shows that the HECS wing maintains a 4% benefit in lift-to-drag over the baseline wing, but the shark wing drops in performance to 4.7% below the baseline configuration. These results suggest there is not a significant difference in the flow physics between the tripped and untripped cases for the baseline and HECS wings. However, this appears not to be the case for the shark wing. Indeed, the oil flow visualization showed that the downstream flow characteristics on the suction side of the Baseline and HECS wings did not greatly differ between the tripped and untripped cases. On the shark wing, however, the downstream flow characteristics on the suction side at an angle of attack of 8 deg were appreciably different from those for the untripped case. Figure 20 shows the resulting surface flow lines on the shark wing with a tripped boundary layer for this angle of attack. Although a separation bubble is no longer apparent, flow separation at the trailing edge appears to creep toward the leading edge as the span is traversed from root to tip. There is also a significant degree of cross flow on the outer span of the wing. It is not clear whether these surface-flow characteristics are due to ineffective boundary layer tripping or if in fact the same conditions would occur at higher Reynolds numbers without tripping. Future detailed

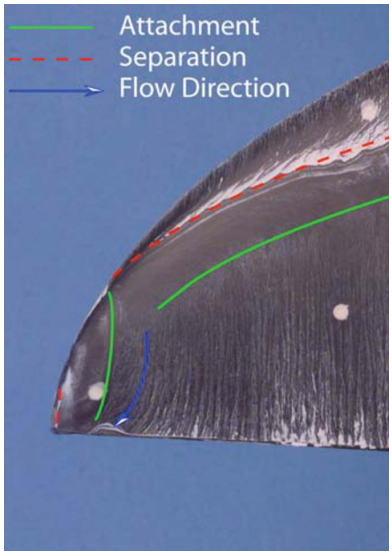

a) Baseline wing

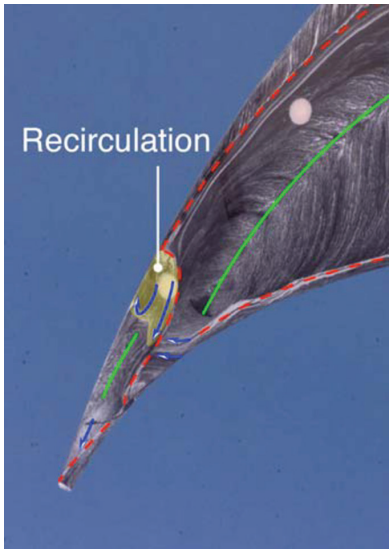

b) HECS wing

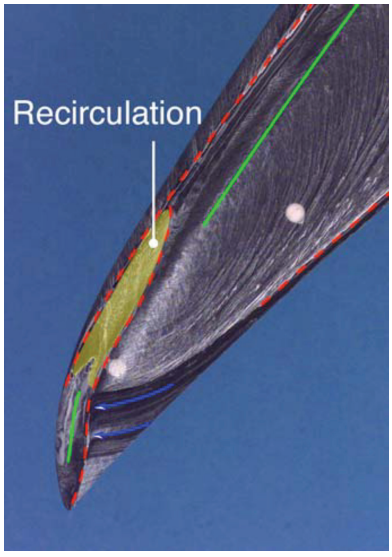

c) Shark wing

Fig. 18 Wing tip oil flow features at an angle of attack of 8 degrees. Solid green lines indicate flow attachment, dashed red lines indicate flow separation, arrowed blue lines indicate flow direction, and yellow transparency indicates a region of flow recirculation.

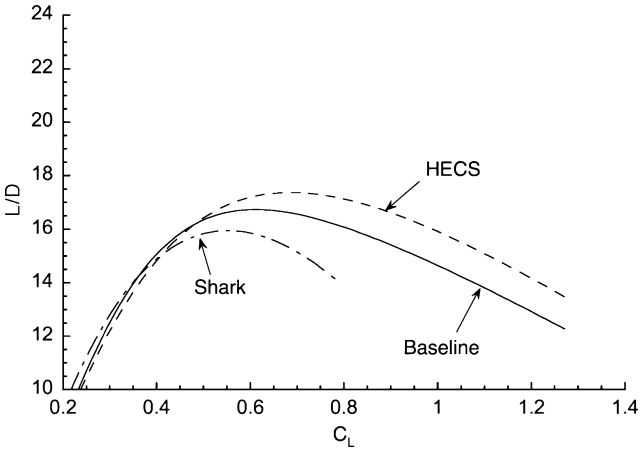

Fig. 19 Lift-to-drag comparison for three configurations with boundary layer tripping (data corrected for tunnel upflow angle).

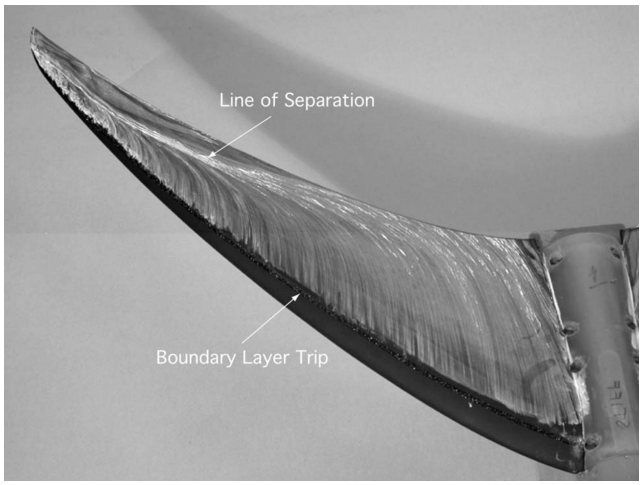

Fig. 20 Oil-flow images of the suction side of the shark wing at an angle of attack of 8 deg with boundary layer tripping.

studies are considered important to determine the flow conditions responsible for the dramatic drop in lift-to-drag performance of the shark wing when boundary layer tripping is employed.

Summary

Four wing configurations inspired by nature were tested to determine performance improvements over a baseline configuration. The gull wing was configured after a seagull in soaring flight, the shark wing was configured after a combination of features on the fins of the great white shark, the WLE wing had a wavy leading edge similar to the head of a scalloped head hammerhead shark, and the HECS wing was configured after the wing shape of a seagull in high-speed gliding flight, with consideration also given to previously published potential theory calculations. All wings had the same planform area and aspect ratio. Wind tunnel force and moment data were gathered and surface oil flow visualizations were performed on each configuration.

Two different comparison techniques were used to evaluate model performance. The results of these techniques compared well with each other. The first technique compared inviscid span efficiency factors for each configuration. The second compared maximum lift-to-drag values. Both comparison techniques show that the shark wing and the HECS wing perform better than the baseline wing, with the shark wing performing the best. A plot of pitching-moment characteristics for each configuration suggests that the shark wing would need significant trimming to eliminate a rather severe pitch recovery moment, reducing the likelihood it would be useful for flight applications. With suction side boundary layer tripping, the HECS wing maintains its percentage improvement over the baseline wing, whereas the shark wing performance falls significantly below that of the baseline wing.

Oil-flow visualizations performed on the smooth untripped models emphasize the expected tip vortex on the baseline wing, but a much more complicated flow pattern is apparent on the tips of the shark and HECS wings. Indications in the shear stress lines are that a counter-rotating pair of vortices persist at the wingtips of each of these models. When the suction side boundary layer of each model is tripped, the laminar separation bubble observed on the smooth models disappears. Under these conditions, the downstream surface flow characteristics on the baseline and HECS wings do not differ appreciably from their untripped cases. This is not the case for the shark wing. For this model, flow reversal on the suction side is observed to become more prominent as the wingtip is approached. It is expected that the significant differences seen in the downstream surface flow characteristics of the shark wing result in its observed performance degradation.

Acknowledgments

The author would like to acknowledge the support and help of John B. Anders, who was originally involved in the development of the model configurations tested and provided advice in the conduct of the research and the development of this article. Special thanks also go to Luther Jenkins, who helped in the understanding and refinement of the balance force and moment data reduction routine.

References

[1]Chiappe, L. M., "The First 85 Million Years of Avian Evolution," *Nature*, Vol. 378, 23 Nov. 1995, pp. 349–355.
[2]Olson, S. L., "The Fossil Record of Birds," *Avian Biology*, edited by D. Farner and J. King, Vol. 3, Academic Press, New York, 1985, pp. 80–217.
[3]Smith, M. P., Sansom, I. J., and Repetski, J. E., "Histology of the First Fish," *Nature*, Vol. 380, April 1996, pp. 702–704.
[4]Long, J. A., "Jawless Wonders: The First Fishes," *The Rise of Fishes*, Johns Hopkins University Press, Baltimore, MD, 1995, pp. 42–63.
[5]Chanute, O., *Progress in Flying Machines*, A Facsimile of the Whole of the First 1894 Edition, Lorenz & Herweg, Long Beach, CA, 1976.
[6]Munk, M. M., "The Minimum Induced Drag of Aerofoils," NACA Report 121, 1923.
[7]Cone, C. D., "The Theory of Induced Lift and Minimum Induced Drag of Non-planar Lifting Systems," NACA Technical Report R-139, 1962.
[8]Oswald, W. B., "General Formulas and Charts for the Calculation of Airplane Performance," NACA Report 408, 1932.
[9]Henderson, W. P., and Holmes, B. J., "Induced Drag—Historical Perspective," SAE Paper 892341, Sept. 1989.
[10]Rokhsaz, K., "A Brief Survey of Wingtip Devices for Drag Reduction," SAE Paper 932574, Sept. 1993.
[11]Van Dam, C. P., "Efficiency Characteristics of Crescent-Shaped Wings and Caudal Fins," *Nature*, Vol. 325, No. 29, 1987, pp. 435–437.
[12]Van Dam, C. P., Vijgen, P. M. H. W., and Holmes, B. J., "Experimental Investigation on the Effects of Crescent Planform on Lift and Drag," *Journal of Aircraft*, Vol. 28, No. 11, 1991, pp. 713–720.
[13]Spillman, J. J., " Wingtip Sails; Progress to Date and Future Developments," *Aeronautical Journal*, Vol. 91, Dec. 1987, pp. 445–453.
[14]Pennycuick, C. J., "Mechanics of Flight," *Avian Biology*, edited by D. Farner and J. King, Vol. 5, Academic Press, New York, 1975, pp. 55–61.
[15]Raspet, A., "Biophysics of Bird Flight," *Science*, Vol. 132, No. 3421, 1960, pp. 191–200.
[16]McMasters, J. H., "An Analytical Survey of Low-Speed Flying Devices: Natural and Man-Made," AIAA Paper 74-1019, Sept. 1974.
[17]Sellers, W. L., and Kjelgaard, S. O., "The Basic Aerodynamics Research Tunnel—A Facility Dedicated to Code Validation," AIAA Paper 88-1997, 1988.
[18]Smith, S. C., "A Computational and Experimental Study of Nonlinear Aspects of Induced Drag," NASA Technical Paper 3598, Feb. 1996.
[19]Watts, P., and Fish, F. E., "The Influence on Passive, Leading Edge Tubercles on Wing Performance," 12th International Symposium on Unmanned Untethered Submersible Technology, Aug. 2001.
[20]Barlow, J. B., Rae, W. H., and Pope, A., "Forces and Moments From Balance Measurements," *Low-Speed Wind Tunnel Testing*, 3rd ed., Wiley, New York, 1999, pp. 265–271.
[21]Lowry, J. G., and Polhamus, E. C., "A Method for Prediction Lift Increments Due to Flap Deflection at Low Angles-of-Attack in Incompressible Flow," NACA TN-3911, Jan. 1957.
[22]Selig, M. S., Guglielmo, J. J., Broeren, A. P., and Giguere, P., "Summary of Low-Speed Airfoil Data," Vol. 1, SoarTech Pub., Virginia Beach, VA, 1995, (ISBN 0-9646747-1-8).